

Stable Support Recovery of Stream of Pulses with Application to Ultrasound Imaging

Tamir Bendory¹, Avinoam Bar-Zion¹, Dan Adam, Shai Dekel and Arie Feuer

Abstract

This paper considers the problem of estimating the delays of a weighted superposition of pulses, called stream of pulses, in a noisy environment. We show that the delays can be estimated using a tractable convex optimization problem with a localization error proportional to the square root of the noise level. Furthermore, all false detections produced by the algorithm have small amplitudes. Numerical and in-vitro ultrasound experiments corroborate the theoretical results and demonstrate their applicability for the ultrasound imaging signal processing.

I. INTRODUCTION

In many engineering and scientific problems, we acquire data that can be modeled as a weighted super-position of pulses (kernels), and aim to decompose it into its building blocks, frequently called *atoms*. Typical examples are ultrasound imaging [30], [31] and radar [3], where the measurements are echoes of the emitted pulse, that are reflected from different targets. When attempting to decompose the stream of pulses there are two main concerns: the robustness of the estimation and its degree of localization. While the localization of the estimation determines how close is the estimation to the real location of the targets, the robustness of the estimation determines the degree to which reliable reconstruction can be performed under different noise conditions. This paper investigates both the robustness and localization of the decomposition of stream of pulses with application to ultrasound imaging.

Ultrasound imaging is currently one of the most widely-used medical imaging modalities worldwide. The popularity of this modality can be attributed to a variety of appealing characteristics, such as cost-effectiveness, portability and being practically harmless. Although ultrasound scans are sufficiently accurate for many applications, the resolution of this modality is limited by the finite bandwidth of ultrasound probes and the aperture of the transducer which determines the axial and lateral resolution, respectively. The limited resolution of ultrasound scans obscures

¹ These two authors contributed equally to this work.

important details and limits the clinical useability of the modality. Another inherent feature of ultrasound imaging, being a coherent imaging modality, is speckle noise. Biological tissues are characterized by numerous structures much smaller than the wavelength of the ultrasonic pulse. These structures induce local inhomogeneity of the acoustic impedance. As a result, the ultrasonic pulse is reflected from many independent scatterers in each resolution cell, defined by the -6dB of the main beam in the axial, lateral and out-of plane dimensions. The combination of these reflections creates a complicated constructive and destructive interference pattern, named speckle noise. Even though the small reflectors creating the speckle noise can not be resolved, the localization of strong reflectors is important for many clinical application, motivating the development of deconvolution and super-localization methods [23], [1], [22].

The ability of different biological structures to reflect the ultrasonic wave is commonly represented by a 3D function, called the reflectivity function. When assuming weak scattering and linear propagation, the received signal (RF signal) can be modeled as a convolution of the reflectivity function and the point spread function (PSF) of the ultrasound scanner [21]. Even in cases where non-linear propagation is dominant, the convolution model can be assumed to hold for short signal sections. The automatic extraction of such sections from the received RF data was discussed in several papers (e.g [23], [21]). Even though the ultrasonic signal results from a convolution of the 3D PSF and the 3D reflectivity function, the deconvolution problem is usually solved by reducing the dimension of the problem and estimating the hypothetical 1D reflectivity function from each scan line, called a-line.

We consider a signal (scan line) which consists of a stream of pulses, i.e.

$$y[k] = \sum_m c_m g_\sigma[k - k_m] + \eta[k], \quad k \in \mathbb{Z}, \quad c_m \in \mathbb{R}, \quad (\text{I.1})$$

where $g_\sigma[k] := g\left(\frac{k}{\sigma N}\right)$, $g(t)$ is an *admissible* kernel, a notion which is defined in Section II, $1/N$ is the uniform sampling interval, $\sigma > 0$ is a scaling parameter and $\|\eta\|_1 := \sum_k |\eta_k| \leq \delta$ is additive noise. We aim to estimate the true support $K := \{k_m\}$ and the weights $\{c_m\}$ from the measurements $\{y[k]\}$.

The model (I.1) can be represented as a convolution model

$$y[k] = (g_\sigma * x)[k] + \eta[k], \quad (\text{I.2})$$

where $'*$ ' represents a discrete convolution, and

$$x[k] = \sum_m c_m \delta[k - k_m], \quad (\text{I.3})$$

where $\delta[k]$ denotes a Kronecker delta function. Our results can be applied directly to deconvolve richer classes of signals, as elaborated in Section II.

A well-known approach to decompose the signal into its atoms is by using parametric methods such as Prony, MUSIC, Matrix Pencil and ESPRIT [27], [26], [19], [25]. However, the stability of these methods is not well-understood, although some steps towards the study of the non-asymptotic behavior have been taken recently [20], [24]. An alternative way is to exploit standard compressed sensing and sparse representations theorems, relying on the sparsity of the signal [17], [14]. These methods require dictionaries with low coherence, and hence highly limit the resolution of the solution.

Recently, it was shown that under a kernel-dependent separation condition on the support K (see Definition II.1) a signal of the form (I.3) can be estimated robustly by solving a ℓ_1 minimization problem [8]. This fundamental result is presented in Theorem II.5. This paper builds on the results of [8], expands some theoretical results and then demonstrates the utility of the approach to ultrasound signal processing. From the theoretical perspective, we follow [18] and derive new results, revealing that the recovery of the ℓ_1 minimization is well-localized. That is to say, the support of the recovered signal is clustered around the support of the underlying signal (I.3) as presented in Theorem II.10. The proof relies on the existence of a special interpolating function, constructed as a super-position of the kernel and its derivatives. Similar techniques were developed in the field of sparse recovery, and specifically as the pillars of the super-resolution theory [9], [10], [29], [13], [2], [6], [7], [4], [5].

Additionally, we validate our theoretical results using ultrasound imaging experiments. These experiments include both numerical simulations and in-vitro phantom scans. The numerical simulations enable the validation of the main result presented in this paper using numerous reflectivity functions with varying spacings and amplitudes. On the other hand, the phantom scans were used to test this method under the conditions of real ultrasound signals and a reflectivity function with known geometry. Together these experiments corroborate the theoretical results and show their relevance to ultrasound signal deconvolution.

The outline of this paper is as follows. In section II, we recall the results of [8] and present our main theoretical result. Section III is devoted to the proof of the localization result. Section IV describes the setup of the experiments we have conducted and presents the results, and Section V concludes the work and outlines some possible future research directions.

II. MAIN RESULT

In a previous work [8], it was shown that robust recovery of a signal (I.3) from a stream of pulses (I.2) is possible if the support K is sufficiently separated and the convolution kernel $g(t)$ meets some mild localization properties. To this end, we recall two fundamental definitions:

Kernels	Gaussian:= $e^{-\frac{t^2}{2}}$	Cauchy:= $\frac{1}{1+t^2}$
C_0	1.22	1
C_1	1.59	1
C_2	2.04	2
C_3	2.6	5.22
$g^{(2)}(0)$	-1	-2
empirical ν	1.1	0.45

TABLE II.1

The table presents the numerical constants of the global property in Definition II.2 for the Gaussian and Cauchy kernels. Additionally, we evaluated by numerical experiments the minimal empirical value of ν , the separation constant of Definition II.1 for each kernel.

Definition II.1. A set of points $K \subset \mathbb{Z}$ is said to satisfy the minimal separation condition for a kernel-dependent $\nu > 0$, a given scaling parameter $\sigma > 0$ and sampling spacing $1/N > 0$ if

$$\min_{k_i, k_j \in K, i \neq j} |k_i - k_j| \geq N\nu\sigma.$$

Definition II.2. A kernel g is admissible if it has the following properties:

- 1) $g \in \mathcal{C}^3(\mathbb{R})$, is real and even.
- 2) Global property: There exist constants $C_\ell > 0, \ell = 0, 1, 2, 3$ such that $|g^{(\ell)}(t)| \leq C_\ell / (1 + t^2)$, where $g^{(\ell)}(t)$ denotes the ℓ^{th} derivative of g .
- 3) Local property: There exist constants $0 < \varepsilon, \beta < \nu$ such that
 - a) $g(t) > 0$ for all $|t| \leq \varepsilon$ and $g(t) < g(\varepsilon)$ for all $|t| > \varepsilon$.
 - b) $g^{(2)}(t) < -\beta$ for all $|t| \leq \varepsilon$.

Remark II.3. Two prime examples for admissible kernels are the Gaussian kernel $g(t) = e^{-\frac{t^2}{2}}$ and Cauchy kernel $g(t) = \frac{1}{1+t^2}$. The numerical constants associated with those kernel are presented in Table II.1.

Remark II.4. The global property in Definition II.2 can be somewhat weakened to $|g^{(\ell)}(t)| \leq C_\ell / (1 + |t|^{1+s})$ for some $s > 0$. In this case, the separation condition would become dependent on s .

The kernel-dependent separation constant ν is defined as the minimal constant guaranteeing the existence of some interpolating function as described in Section 3.1 of [8] (see Lemma III.1). The minimal separation constant for the Cauchy and Gaussian kernels was evaluated numerically to be 0.45 and 1.1 (see Table II.1).

In this paper, we consider recovery by solving the following tractable convex optimization problem:

$$\min_{\tilde{x} \in \ell_1(\mathbb{Z})} \|\tilde{x}\|_1 \quad \text{subject to} \quad \|y - (g_\sigma * \tilde{x})\|_1 \leq \delta. \quad (\text{II.1})$$

Denote the solution of (II.1) as

$$\hat{x}[k] = \sum_n \hat{c}_n \delta[k - \hat{k}_n], \quad \hat{K} := \{\hat{k}_n\}. \quad (\text{II.2})$$

We are ready now to state the main result of [8]. This result shows that the recovery error of (II.1) is proportional to noise level.

Theorem II.5. *Let y be of the form of (I.1) and let g be an admissible kernel as defined in Definition II.2. If the signal's support K satisfies the separation condition of Definition II.1 for $\sigma, N > 0$, then the solution \hat{x} of (II.1) satisfies (for sufficiently large ν)*

$$\|\hat{x} - x\|_1 \leq \frac{16\gamma^2}{\beta} \delta,$$

where

$$\gamma = \max\{N\sigma, \varepsilon^{-1}\}. \quad (\text{II.3})$$

Corollary II.6. *In the noiseless case $\delta = 0$, (II.1) results in exact recovery.*

Remark II.7. A tighter bound on the recovery error is presented in Theorem 2.12 in [8]. For the sake of clarity, we presented here a simplified version of the stability result.

Remark II.8. We chose to focus on the univariate results as we aim to apply it on 1D ultrasound scans. However, we stress that an equivalent result holds for the bivariate case. Namely, the recovery error is proportional to the noise level δ and depends on the kernel localization properties.

For a fix $k_m \in K$, let

$$\mathbb{Z}_m := \{k \in \mathbb{Z} : |k - k_m| \leq N\varepsilon\sigma\}. \quad (\text{II.4})$$

Accordingly, we define the partition of \mathbb{Z} to disjoint subsets $\mathbb{Z} = \mathbb{Z}_{near} \cup \mathbb{Z}_{far}$, where

$$\begin{aligned} \mathbb{Z}_{near} &:= \cup_{\{m: k_m \in K\}} \mathbb{Z}_m, \\ \mathbb{Z}_{far} &:= \mathbb{Z}_{near}^C \\ &= \{k \in \mathbb{Z} : |k - k_m| > N\varepsilon\sigma, \forall k_m \in K\}. \end{aligned} \quad (\text{II.5})$$

This paper focuses on the localization properties of the solution of (II.1). Therefore, we present the following important corollary which states that the superfluous spikes, far away from the sought signal, have low amplitudes.

Corollary II.9. *Let us define the set $\hat{K}_{far} := \mathbb{Z}_{far} \cap \hat{K}$, where \mathbb{Z}_{far} and \hat{K} are given in (II.5) and (II.2), respectively. Under the conditions of Theorem II.5, we have*

$$\sum_{\{n: \hat{k}_n \in \hat{K}_{far}\}} |\hat{c}_n| \leq \frac{16\gamma^2}{\beta} \delta.$$

Proof: By definition, $x[k] = 0$ for all $k \in \hat{K}_{far}$. Therefore, using Theorem II.5 we get

$$\begin{aligned} \sum_{\{n: \hat{k}_n \in \hat{K}_{far}\}} |\hat{c}_n| &= \sum_{\{n: \hat{k}_n \in \hat{K}_{far}\}} \left| \hat{x}[\hat{k}_n] - x[\hat{k}_n] \right| \\ &\leq \sum_{k \in \mathbb{Z}} |\hat{x}[k] - x[k]| \\ &\leq \frac{16\gamma^2}{\beta} \delta. \end{aligned}$$

■

Although the optimization problem (II.1) is defined on a discrete grid, it was proven that it converges to a solution on the continuum (in the sense of measures) as the discretization becomes finer [28]. Additionally, the behavior of the discrete optimization problem solution, when the underlying signal is defined on a compact domain is analyzed in detail in [15], [16].

We want to emphasize that our model can be extended to other types of underlying signals, not necessarily a spike train as in (I.3). For instance, suppose that the underlying signal itself is a stream of pulses, namely a signal of the form $\hat{x}[k] = \sum c_m \dot{g}_{\sigma_2}[k - k_m]$. In this case, the measurements are given as $y[k] = (g_{\sigma_1} * \dot{g}_{\sigma_2} * x)[k]$ where x is a signal of the form of (I.3). Therefore, our results hold immediately if the convolution kernel $\tilde{g}[k] = (g_{\sigma_1} * \dot{g}_{\sigma_2})[k]$ meets the definition of admissible kernel and the signal's support K satisfies the associated separation condition. For instance, if g and \dot{g} are both Gaussian kernels with standard deviations of σ_1 and σ_2 , then \tilde{g} is also Gaussian with standard deviation of $\sigma = \sqrt{\sigma_1^2 + \sigma_2^2}$ and thus obeys the definition of admissible kernel. In the continuous case (i.e. $N \rightarrow \infty$), our model can be extended to splines as well with moderate additional information.¹

The main theoretical contribution of this paper is the following theorem, stating that under the separation condition, for any $k_m \in K$ with sufficiently large amplitude c_m , there exists a close $\hat{k}_m \in \hat{K}$. Namely, the solution of (II.1) locates a spike near any spike of the underlying signal. In [18], the support detection for the super-resolution problem was examined by convex optimization tools. We follow this line of research and present the main theorem of this paper, as follows:

¹In this paper we present the theory for discrete signals. However, in [8] the noise-free result is developed on the continuum. The extension to splines involves the derivation of the measurements, so it holds only for the continuous case.

Theorem II.10. *Let y be of the form of (I.1) and let g be an admissible kernel as defined in Definition II.2. If the signal support K satisfies the separation condition of Definition II.1, then the solution \hat{x} of the convex program (II.1) has the following property: For any m such that $|c_m| > \frac{16\gamma^2}{\beta}\delta$ there exists a $\hat{k}_m \in \hat{K}$ such that*

$$|k_m - \hat{k}_m| \leq \frac{8\gamma^2}{\beta} \sqrt{\frac{g(0)\delta}{\left(|c_m| - \frac{16\gamma^2}{\beta}\delta\right)}}.$$

The localization result of Theorem II.10 cannot be derived directly from the robustness result of Theorem II.5. For instance, suppose that the amplitude c_m and the noise level δ are of the same order. Then, Theorem II.10 guarantees that there exists at least one location $\hat{k}_m \in \hat{K}$ obeying $|\hat{k}_m - k_m| \leq C$ for some kernel-dependent constant C . This localization error can not be inferred from the robustness result.

III. PROOF OF THEOREM II.10

The main pillar of the proof is the existence of a special superposition of the kernel and its first derivative which satisfies some interpolation properties. This function is frequently called the *dual certificate*. We begin by stating the following Lemma from [8]:

Lemma III.1. *Suppose that the set $T := \{t_m\} \subset \mathbb{R}$ obeys the separation condition*

$$\min_{t_i, t_j \in T, i \neq j} |t_i - t_j| \geq \nu\sigma,$$

for some constant $\nu > 0$. Let $\{u_m\} \in \pm 1$ be a sign sequence and let $g(t)$ be an admissible kernel as defined in Definition II.2. Then, there exists a set of coefficients $\{a_m\}$ and $\{b_m\}$ such that the function

$$q(t) = \sum_m a_m g\left(\frac{t - t_m}{\sigma}\right) + b_m g^{(1)}\left(\frac{t - t_m}{\sigma}\right),$$

satisfies $\|q\|_\infty = \max_{t \in \mathbb{R}} |q(t)| \leq 1$ and interpolates the sequence $\{u_m\}$ on $\{t_m\}$, namely $q(t_m) = u_m$ for all $t_m \in T$. Additionally, for all t satisfying $|t - t_m| \leq \varepsilon\sigma$ for some $t_m \in T$, we have $|q(t)| \leq 1 - \frac{\beta(t - t_m)^2}{4g(0)\sigma^2}$.

We will also need the following result:

Lemma III.2. *Let the signal support K satisfy the separation condition of Definition II.1 and let $\hat{K}_{near} := \mathbb{Z}_{near} \cap \hat{K}$, where \mathbb{Z}_{near} is defined in (II.5) and \hat{K} in (II.2). Then,*

$$\sum_{\{n: \hat{k}_n \in \hat{K}_{near}\}} |\hat{c}_n| d^2(\hat{k}_n, K) \leq \frac{64g(0)\gamma^4}{\beta^2} \delta,$$

where $d(k, K) := \min_{k_m \in K} |k_m - k|$ and γ and δ are defined in (II.3) and (I.1), respectively.

Proof: Let $u_m = \text{sign}(c_m)$, where $\text{sign}(z) := \frac{z}{|z|}$ and $q(t)$ the corresponding function as defined in Lemma III.1. Denoting $q[k] = q(k/N)$, $k \in \mathbb{Z}$ we get from Lemma III.1 for all $k \in \mathbb{Z}_{near}$

$$|q[k]| \leq 1 - \frac{\beta(k - k_m)^2}{4g(0)(N\sigma)^2},$$

where by definition of \mathbb{Z}_{near} there exists $k_m \in K$ such that $|k - k_m| \leq \varepsilon N\sigma$. Then,

$$\begin{aligned} \sum_{k \in \mathbb{Z}_{near}} q[k] \hat{x}[k] &= \sum_{k \in \hat{K}_{near}} q[k] \hat{x}[k] \\ &\leq \sum_{\{n: \hat{k}_n \in \hat{K}_{near}\}} |\hat{c}_n| \left| q \left[\hat{k}_n \right] \right| \\ &\leq \sum_{\{n: \hat{k}_n \in \hat{K}_{near}\}} |\hat{c}_n| \left(1 - \frac{\beta d^2 \left(\hat{k}_n, K \right)}{4g(0)(N\sigma)^2} \right). \end{aligned} \quad (\text{III.1})$$

Since by Lemma III.1 we have $\|q\|_\infty := \max_{k \in \mathbb{Z}} |q[k]| \leq 1$ we use Theorem II.5 to observe

$$\begin{aligned} \left| \sum_{k \in \mathbb{Z}_{near}} q[k] (\hat{x}[k] - x[k]) \right| &\leq \sum_{k \in \mathbb{Z}} |q[k]| |\hat{x}[k] - x[k]| \\ &\leq \|q\|_\infty \|\hat{x} - x\|_1 \\ &\leq \frac{16\gamma^2}{\beta} \delta. \end{aligned} \quad (\text{III.2})$$

Then, combining (III.1) and (III.2) into

$$\sum_{k \in \mathbb{Z}_{near}} q[k] \hat{x}[k] = \sum_{k \in \mathbb{Z}_{near}} q[k] (\hat{x}[k] - x[k]) + \sum_{k \in \mathbb{Z}_{near}} q[k] x[k].$$

we get

$$\begin{aligned} \sum_{\{m: k_m \in K\}} |c_m| - \frac{16\gamma^2}{\beta} \delta &\leq \sum_{k \in \mathbb{Z}_{near}} q[k] (\hat{x}[k] - x[k]) + \sum_{k \in \mathbb{Z}_{near}} q[k] x[k] \\ &\leq \sum_{\{n: \hat{k}_n \in \hat{K}_{near}\}} |\hat{c}_n| \left(1 - \frac{\beta d^2 \left(\hat{k}_n, K \right)}{4g(0)(N\sigma)^2} \right), \end{aligned}$$

where we used the fact that $\sum_{k \in \mathbb{Z}_{near}} q[k] x[k] = \sum_{\{m: k_m \in K\}} |c_m|$. Furthermore, since by (II.1) we have

$$\|x\|_1 = \sum_{\{m: k_m \in K\}} |c_m| \geq \|\hat{x}\|_1 = \sum_{\{n: \hat{k}_n \in \hat{K}\}} |\hat{c}_n| \geq \sum_{\{n: \hat{k}_n \in \hat{K}_{near}\}} |\hat{c}_n|,$$

we conclude that

$$\sum_{\{n: \hat{k}_n \in \hat{K}_{near}\}} |\hat{c}_n| - \frac{16\gamma^2}{\beta} \delta \leq \sum_{\{n: \hat{k}_n \in \hat{K}_{near}\}} |\hat{c}_n| \left(1 - \frac{\beta d^2 \left(\hat{k}_n, K \right)}{4g(0)(N\sigma)^2} \right)$$

and

$$\begin{aligned} \sum_{\{n: \hat{k}_n \in \hat{K}_{near}\}} |\hat{c}_n| d^2(\hat{k}_n, K) &\leq \frac{64g(0)\gamma^2 (N\sigma)^2}{\beta^2} \delta \\ &\leq \frac{64g(0)\gamma^4}{\beta^2} \delta. \end{aligned}$$

This concludes the proof. \blacksquare

We are now ready to prove Theorem II.10. Fix $k_m \in K$, let \mathbb{Z}_m be as in (II.4) and let $\hat{K}_m := \mathbb{Z}_m \cap \hat{K}$. Since $\varepsilon < \nu$ (the separation constant), $\mathbb{Z}_m \cap K = \{k_m\}$. Hence, by Theorem II.5 we get

$$\begin{aligned} \left| c_m - \sum_{\{n: \hat{k}_n \in \hat{K}_m\}} \hat{c}_n \right| &= \left| \sum_{k \in \mathbb{Z}_m} x[k] - \hat{x}[k] \right| \\ &\leq \sum_{k \in \mathbb{Z}_m} |x[k] - \hat{x}[k]| \\ &\leq \sum_{k \in \mathbb{Z}} |x[k] - \hat{x}[k]| \\ &\leq \frac{16\gamma^2}{\beta} \delta. \end{aligned}$$

If $|c_m| > \frac{16\gamma^2}{\beta} \delta$, then \hat{K}_m is not an empty set, namely, there exists at least one $\hat{k}_n \in \hat{K}$ so that $|\hat{k}_n - k_m| \leq N\varepsilon\sigma$. Additionally, by the triangle inequality $|c_m| - \frac{16\gamma^2}{\beta} \delta \leq \sum_{\{n: \hat{k}_n \in \hat{K}_m\}} |\hat{c}_n|$. Let $\bar{d} = \min_{\hat{k}_n \in \hat{K}_m} |\hat{k}_n - k_m|$. Then, using Lemma III.2 we directly get

$$\begin{aligned} \bar{d}^2 &\leq \frac{64g(0)\gamma^4}{\beta^2 \sum_{\{n: \hat{k}_n \in \hat{K}_{near}\}} |\hat{c}_n|} \delta \\ &\leq \frac{64g(0)\gamma^4}{\beta^2 \left(|c_m| - \frac{16\gamma^2}{\beta} \delta \right)}. \end{aligned}$$

This concludes the proof.

IV. ULTRASOUND EXPERIMENTS

The theoretical results were validated in a series of numerical and *in-vitro* experiments. In the *in-vitro* experiments, a mechanical phantom with a known geometry was scanned using a single-element ultrasound transducer. The same setup was used in order to estimate the PSF for the numerical experiments. An unfocused, single-element Panamatrix transducer with 0.375" diameter was used in all the scans (A3265-SU, Whaltham, MA). This transducer was operated in a transmitter-receiver pulse-echo configuration. A single channel arbitrary function generator (8024, Tabor Electronics, Tel-Hanan, Israel) was used to drive the transducer with a pulse containing adjustable number

of sinusoidal cycles. The function generator was operated at 4MHz during all the experiments described below. The received RF-lines were sampled at a rate of 100MHz using a 14bit digitizer (CS8427 ,Gage, Lockport, IL). In order to protect the digitizer from over-voltage the received RF data was passed through an external diplexer (RDX-6, RITEC, Warwick, RI). A diagram of the experimental setup can be found in Figure IV.3a .The recorded RF signals were loaded into a personal computer and analyzed using dedicated MATLAB® code (The Mathworks, Natic, MA).

A. Numerical Simulation

In order to emulate a realistic RF line, the ultrasound pulse used in the numerical simulations was the pulse-echo signal reflected from a thick perspex sheet immersed in a water tank. Pulses with two and three cycles were transmitted and the reflected echos were received and recorded. It is assumed that the received pulse measured this way is a reliable estimation for the convolution kernel in equation (I.2). The simulated ultrasound signal was produced according to the following steps. First, the simulated reflectivity signal was produced. The reflectivity signals were comprised of a series of evenly-spaced reflectors with random amplitudes uniformly distributed between $\pm[5, 10]$. Different separations enabled the comparison between the localization results achieved for different reflectors density. Second, the simulated reflectivity function was convolved with the estimated kernel. Different levels of SNR were simulated by adding a Gaussian white noise to the resulting signal. 100 simulated signals were produced for each combination of separation and SNR conditions.

Although the RF pulses as modulated signals do not decay monotonously, the demodulated signals and their envelopes are compatible with the model described above (I.1). Therefore, the simulated signals were demodulated by multiplication with the carrier frequency and application of a low-pass FIR filter. Following the demodulation, the optimization problem (II.1) was solved using CVX, a toolbox for specifying and solving convex programs [12]. The value of δ was selected so that $\|\eta * g\|_{\ell_1} \leq \delta$ in accordance with equation (II.1) and adjusted according to the SNR level. Examples of the original and reconstructed reflectivity functions produced using a two-cycle pulse and a three-cycle pulse with SNR of 23 dB are presented in Figures IV.1(a) and IV.1(b), respectively. This example demonstrates how the localization of the estimation decreases and the locations of the recovered reflectors get further from their original locations as the width of the convolution kernel increases.

In order to quantify the performance of the localization algorithm, the localization error was measured for different levels of SNR using two-cycle three-cycle pulses. The localization error was defined as the distance between the real location of each reflector and the location of the closest reflector in the solution. The results of this analysis can be seen in Figure IV.2. For each separation and SNR level, subplots (a) and (b) present the mean localization error of

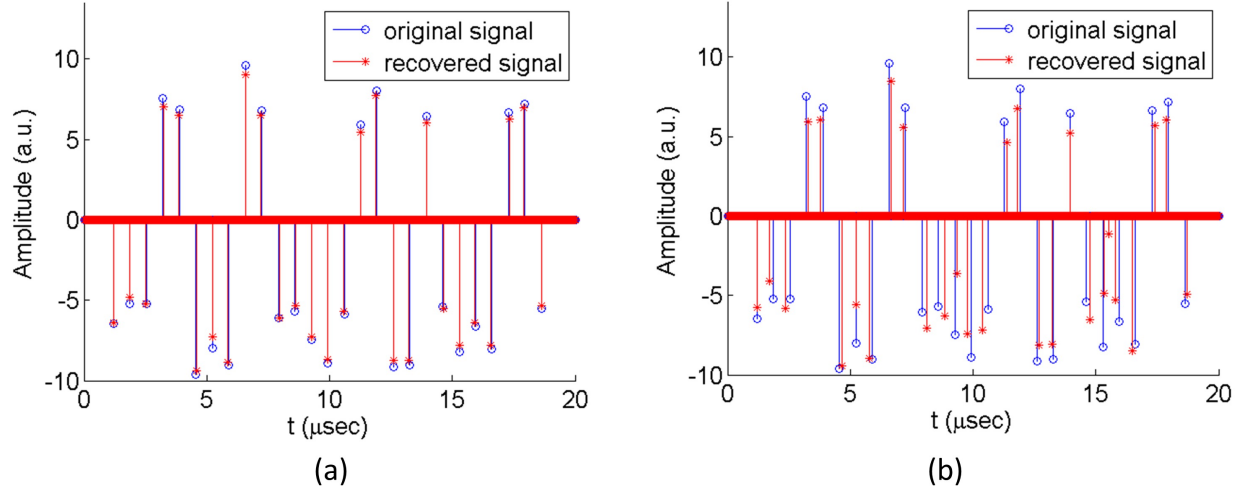


Fig. IV.1. Representative results of numerical simulation experiments: reflectivity estimates are presented against true reflectors locations, for two different pulse lengths at SNR = 23dB. (a) Results from a two-cycle pulse, (b) results from a three-cycle pulse.

the simulations using two-cycle and three-cycle pulses, respectively. The mean localization error of the simulations produced using the two-cycle pulse is relatively small for SNR levels greater than 15 dB and increases for small separation intervals. In contrast, the mean localization error of the simulations produced using the three-cycle pulse is markedly higher as the reflectors are not sufficiently separated. Subplots (c) and (d) present the standard deviation of the localization error for each separation and SNR level. When measuring the mean localization error most of the localization error is averaged out, indicating that the solutions are clustered around the real locations. The measured standard deviation values are almost one order of magnitude higher than these of the mean localization error. Hence, the standard deviation of the localization error is a much more suitable criterion for localization loss.

B. In-vitro experiment

In order to validate the algorithm's ability to reliably detect the location of reflectors in real ultrasound RF scans, a phantom with a known geometry was constructed. Similar to the phantom used in [1], the phantom was constructed from parallel layers of perspex and polycarbonate held together by a rigid frame. The dimensions of the phantom in the direction orthogonal to the transmitted beam are much larger than each layer's thickness making it a 1D phantom. The thickness of the layers and the distance between them were measured in advance and are detailed in Table IV.1. The large differences between the impedance of the solid perspex and polycarbonate sheets and the

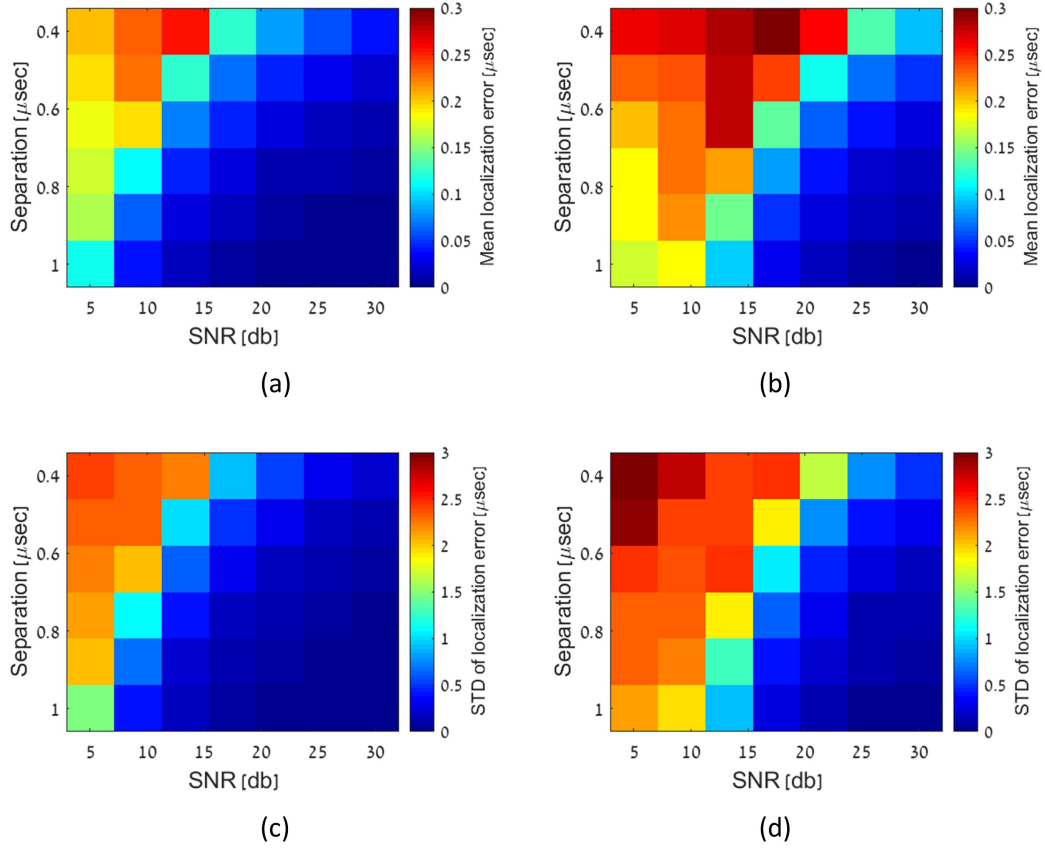


Fig. IV.2. Quantification of the numerical simulations: In subplots (a) and (b) the mean localization error is presented for each separation and SNR level for simulations produced using a two-cycle pulse and a three-cycle pulse, respectively. In subplots (c) and (d) the standard deviation of the localization error is presented for simulations produced using a two-cycle pulse and a three-cycle pulse, respectively.

water in which they are submerged produce strong acoustic reflectors in each interface. Therefore, only a fraction of the acoustic energy penetrates beyond the first few layers. Due to the fast decay of the signal only the first five layers (six reflectors) were relevant to our analysis.

The phantom was design to enable the validation of the localization algorithm under a various of relevant conditions. The thickness of the Perspex and polycarbonate layers and the distance between them are of the same order as the wavelength of the transmitted pulse. Therefore, the RF-lines can have variable levels of echo interference as function of the number of cycles transmitted in each pulse. Additionally, although the alternating high reflectivity values do not mimic a specific tissue of organ, they enable the validation of the localization algorithm under various

Number of layer	Layer Thickness (mm)	Distance between layers (mm)
1	3 (Perspex)	
		1.3
2	1 (polycarbonate)	
		0.9
3	1.8 (Perspex)	
		1.3
4	1 (polycarbonate)	
		1.5
5	1.8 (Perspex)	
		1.3
6	3 (Perspex)	

TABLE IV.1

DIMENSIONS OF THE PERSPEX-POLYCARBONATE PHANTOM. THE GAP BETWEEN EACH PERSPEX/ POLYCARBONATE LAYER WAS FILLED WITH WATER AS THE PHANTOM WAS SUBMERGED IN A WATER TANK.

SNR values.

The transducer was inserted through one of the walls of the a dedicated water tank filled with deionized water at room temperature (see Figure IV.3(b)). The phantom was placed in the center of the tank and was aligned to be perpendicular to the beam by changing its orientation until a maximal echo amplitude was achieved. Pulses with one to four cycles were transmitted and the reflected echos were received and recorded. The pulses containing different number of transmitted cycles produced signals with slightly different peak amplitudes. In order to achieve comparable base-ground SNR level, white Gaussian noise was added to the received signal resulting in identical SNR of 41dB. The pulse shape was estimated from the echo reflected from the first Perspex layer, which was thick enough to ensure the separation of the first echo from the consecutive reflections. Later, different levels of SNR were achieved by adding white Gaussian noise with different standard deviation to the resulting signals.

The RF signals are demodulated as described in Section IV-A. After the demodulation, the optimization problem (II.1) was solved using CVX [12]. Complex reflectivity function values were enabled in order to facilitate the incorporation of phase delays into the signal model as proposed in [31]. The value of the noise level parameter δ was selected so that $\|\eta * g\|_{\ell_1} \leq \delta$ in accordance with equation (II.1) and adjusted according to the SNR level. The reflectivity function estimates were compared against the true location of the reflectors used as a reference. The absolute value of the estimated reflectivity function is presented along with the location of the reflectors. Since both

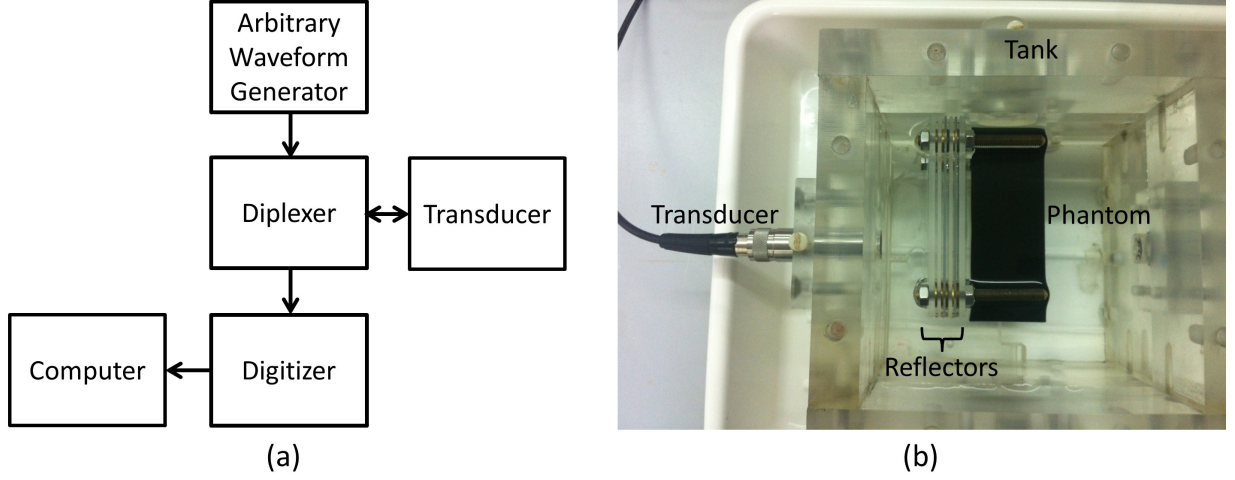


Fig. IV.3. Experimental set-up. (a) a diagram of the experimental setup. (b) the mechanical phantom placed in front of the transducer.

the attenuation and acoustic reflections gradually reduce the energy of the traveling wave, there was no attempt to compare the estimated magnitude of the reflectivity function to that of the phantom.

Two RF-lines received after transmitting a single-cycle pulse and a four-cycle pulse are presented in Figures IV.4(a) and IV.4(b), respectively. The estimated reflectivity function correlates well with the structure of the phantom and the different interfaces originally masked by the interference of the pulses are revealed. When wider pulses are transmitted, the kernel-dependent minimal separation condition demands greater separation of the strong reflectors. As a result, better localization of the reflectivity estimates are achieved for shorter pulses, containing one or two cycles. Since the reflected energy is not compensated after each layer transition, the amplitude of the estimated reflectivity function decrease with depth. As the pulse energy decrease with depth, the local SNR decreases, resulting in reduced localization of deeper phantom layers.

In order to quantify the performances of the localization algorithm, the localization error was measured for different levels of SNR and for pulses containing different number of cycles. 100 experiments were performed for each SNR level and pulse length combination. A representative example of an estimation performed with different SNR levels can be found in Figure IV.5. As the SNR decreases the localization error increases. For sufficiently large SNR, the support of the solution (of the discrete optimization problem) is tightly clustered around the true support (on the continuum). This phenomenon is typical for ℓ_1 minimization problems (see the analysis on compact domains in [15], [16]).

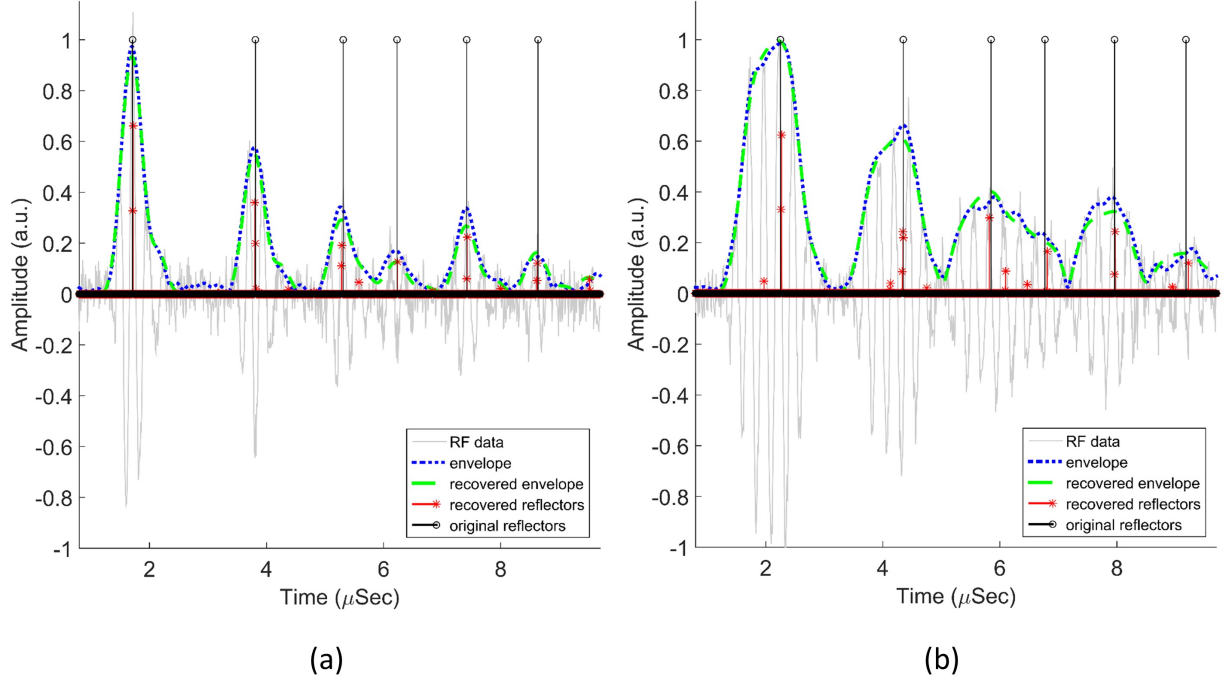


Fig. IV.4. Representative results of phantom experiments: reflectivity estimates are presented against true reflectors' location, for two different pulse lengths at SNR = 23dB. (a) Results from a single cycle pulse (b) Results from a four cycle pulse. Each subplot contains the received RF-line, the estimated and the original reflectivity functions and the original and reconstructed envelopes of the signal.

It is important to note that the measured SNR reflects the SNR level for the closest reflector. The signal resulting from reflectors located further from the transducer has lower SNR. As the noise level increases the signal reflected from some of the deeper reflector drops below the noise floor. Our main result in Theorem II.10 do not guarantee the detection and localization of the reflectors in these cases.

The reduced localization for low SNR levels and long pulses is reflected by higher standard deviation of the localization error (see Figure IV.5(c)). When transmitting short pulses the localization of the reflectors remains stable even for low SNR levels. The standard deviation of the localization error for each SNR level is higher for longer pulses, as predicted.

Following Corollary II.9, the solution \hat{x} can include some false reflectors detections of small amplitude, far from the real location of the reflectors. In order to quantify the amplitude of these estimation artifacts as a function of the SNR level, the mean value of $\|\hat{x}\|_1$ between the first and the second reflector was evaluated (see gray region

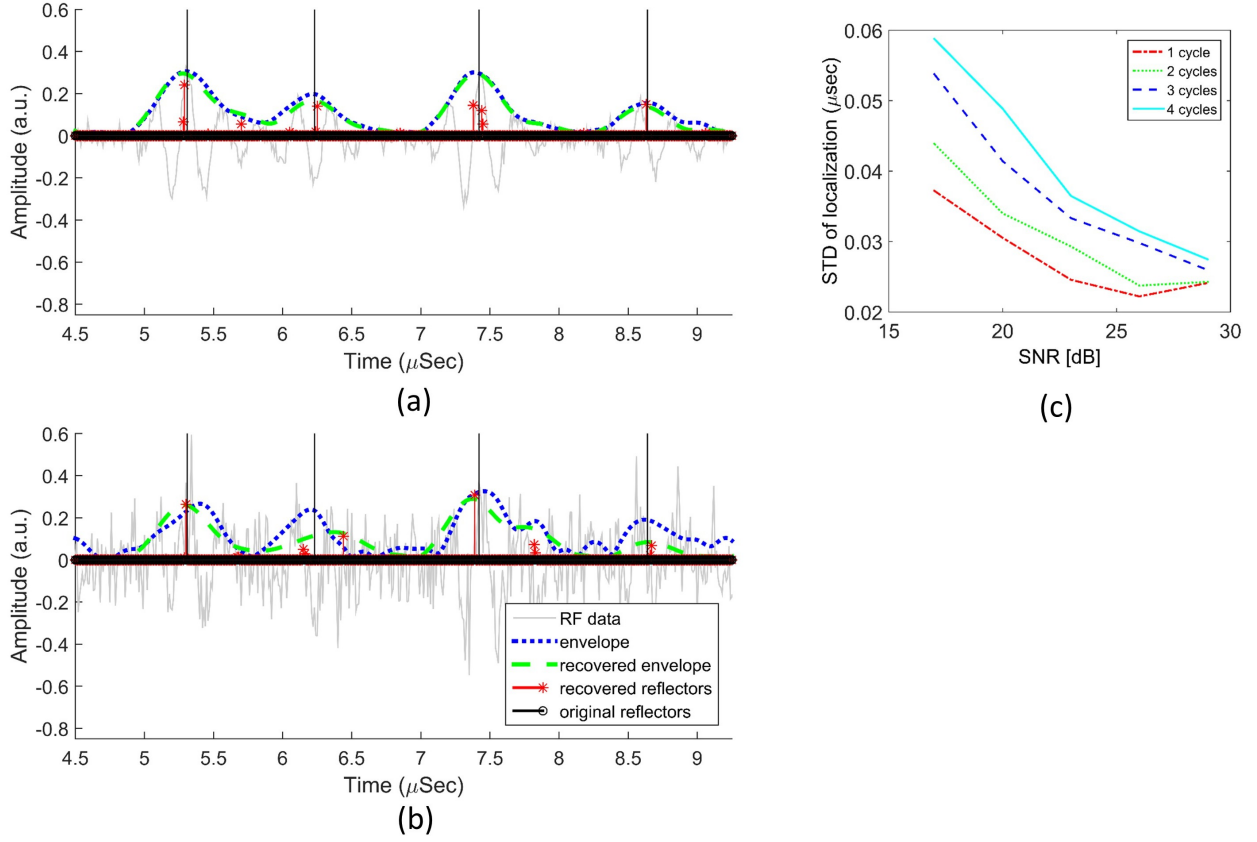


Fig. IV.5. Localization reduction for low SNR levels: reflectivity estimates of the 3rd - 6th reflectors are presented against true reflectors location, for single cycle pulse at two different SNR values. Subplot (a) shows the results for SNR = 29dB and subplot (b) shows the results for SNR = 17dB. The standard deviation of the localization error as function of the SNR is presented in subplot (c). 100 experiments were performed for every combination of SNR level and pulse length.

in Figure IV.6(a)). The minimal distance from each reflector used in this analysis was two wavelength. Since the distance between the first and second reflections in the measured (low-resolution) signal is reduced for longer pulses, the analysis was performed for the single cycle measurements. A monotonic reduction in the mean amplitude of the false detections as a function SNR was measured as presented in Figure IV.6(b). This inverse relation between the SNR and the estimation artifacts corroborates Corollary II.9.

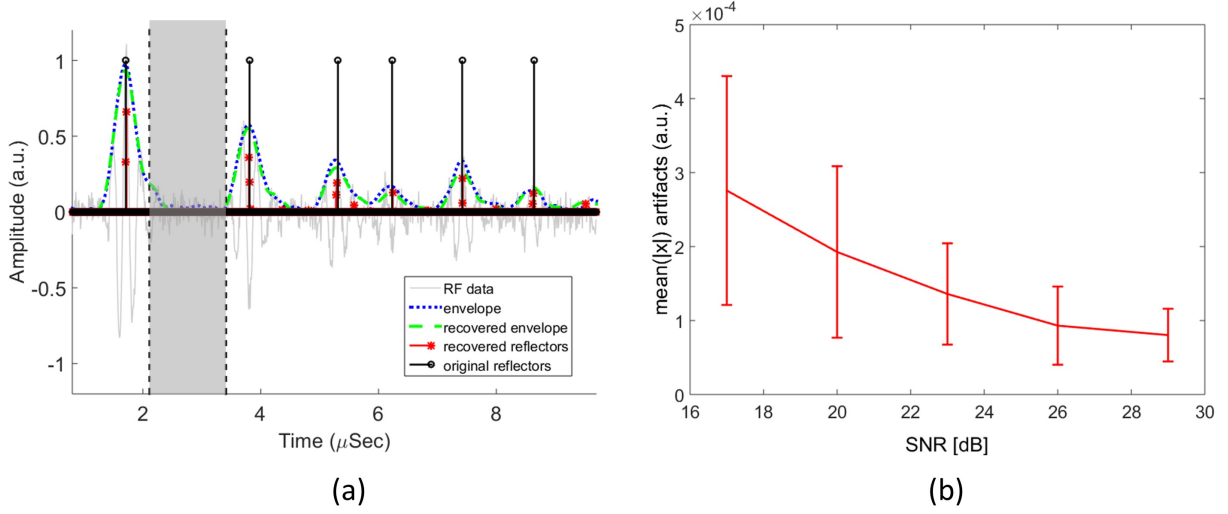


Fig. IV.6. False detections: The mean value of non-zero reflectivity estimates located between the first and second reflector but far from the true location of these reflectors (gray region in subplot (a)) was evaluated in order to quantify the estimation artifacts level (subplot (b)) as a function of the SNR.

V. CONCLUSIONS

In this work, we derived theoretical results regarding the localization properties of convex optimization technique for decomposition of a stream of pulses. This highlights the appealing properties of the convex optimization approach for the decomposition of stream of pulses, as proved and discussed in previous works [8], [5].

From the theoretical perspective, we demonstrated the effectiveness of the separation condition. Furthermore, it is clear that without some separation, no algorithm can decompose a stream of pulses in the presence of noise. However, it is not clear yet that a separation condition as presented in Definition II.1 is necessary, and what is the optimal regularity condition for the recovery by tractable algorithms, such as convex optimization, algebraic methods and iterative algorithms.

The experimental results presented in Section IV corroborate our theoretical results. With sufficient separation of scatterers, the localization degree of strong scatterers was shown to be governed by the noise: the mean and the standard deviation of the localization error increases with the noise level. In both numerical simulations and phantom experiments, for a given SNR level, short pulses produced better localization compared to wider pulses. In addition, the amplitude of artifact scatterers located far from the location of the real scatterers is shown to be small and decrease monotonically with the noise level.

The results presented in this paper have important implications on studies attempting to perform super-resolution on signals that can be modeled as streams of pulses. Specifically, the results of ultrasound deconvolution algorithms based on signal sparsity/compressibility priors can be analyzed and explained. The reliable localization of strong reflectors in ultrasound images has important applications such as the accurate measurement of the intima-media thickness (IMT), the innermost layers of the of an artery, in order to facilitate early detection of plaque formation [32], [33]. Another possible use could be in non-destructive tests. Moreover, the stream of pulses model is a popular model in compressed sensing ultrasound [31], [11] and compressed sensing radar [3]. Therefore, the presented results have implication on the interpretation of the representations of the signals in these applications.

Acknowledgement. The authors thank Amit Livneh for his help with the in-vitro ultrasound setup.

REFERENCES

- [1] D. Adam and O. Michailovich. Blind deconvolution of ultrasound sequences using nonparametric local polynomial estimates of the pulse. *Biomedical Engineering, IEEE Transactions on*, 49(2):118–131, Feb 2002.
- [2] Jean-Marc Azais, Yohann De Castro, and Fabrice Gamboa. Spike detection from inaccurate samplings. *Applied and Computational Harmonic Analysis*, 2014.
- [3] Omer Bar-Ilan and Yonina C. Eldar. Sub-nyquist radar via doppler focusing. *IEEE Transactions on Signal Processing*, 62(7):1796–1811, 2014.
- [4] T. Bendory, S. Dekel, and A. Feuer. Super-resolution on the sphere using convex optimization. *Signal Processing, IEEE Transactions on*, 63(9):2253–2262, May 2015.
- [5] Tamir Bendory. Robust recovery of positive stream of pulses. *submitted, arXiv preprint arXiv: 1503.08782*, 2015.
- [6] Tamir Bendory, Shai Dekel, and Arie Feuer. Exact recovery of dirac ensembles from the projection onto spaces of spherical harmonics. *Constructive Approximation, to appear*, 2013.
- [7] Tamir Bendory, Shai Dekel, and Arie Feuer. Exact recovery of non-uniform splines from the projection onto spaces of algebraic polynomials. *Journal of Approximation Theory*, 182(0):7 – 17, 2014.
- [8] Tamir Bendory, Shai Dekel, and Arie Feuer. Robust recovery of stream of pulses using convex optimization. *submitted, arXiv preprint arXiv: 1412.3262*, 2014.
- [9] Emmanuel J Candès and Carlos Fernandez-Granda. Super-resolution from noisy data. *Journal of Fourier Analysis and Applications*, 19(6):1229–1254, 2013.
- [10] Emmanuel J Candès and Carlos Fernandez-Granda. Towards a mathematical theory of super-resolution. *Communications on Pure and Applied Mathematics*, 2013.
- [11] Tanya Chernyakova and Yonina C. Eldar. Fourier domain beamforming: The path to compressed ultrasound imaging. *CoRR*, abs/1307.6345, 2013.
- [12] Inc. CVX Research. CVX: Matlab software for disciplined convex programming, version 2.0, August 2012.
- [13] Yohann De Castro and Fabrice Gamboa. Exact reconstruction using beurling minimal extrapolation. *Journal of Mathematical Analysis and applications*, 395(1):336–354, 2012.
- [14] David L Donoho. Compressed sensing. *Information Theory, IEEE Transactions on*, 52(4):1289–1306, 2006.
- [15] Vincent Duval and Gabriel Peyré. Exact support recovery for sparse spikes deconvolution. *Foundations of Computational Mathematics*, pages 1–41, 2013.

- [16] Vincent Duval and Gabriel Peyré. Sparse spikes deconvolution on thin grids. *arXiv preprint arXiv:1503.08577*, 2015.
- [17] Michael Elad. *Sparse and redundant representations: from theory to applications in signal and image processing*. Springer, 2010.
- [18] Carlos Fernandez-Granda. Support detection in super-resolution. In *10th Sampling Theory and Applications (SAMPTA)*, pages 145–148, 2013.
- [19] Yingbo Hua and Tapan K Sarkar. Matrix pencil method for estimating parameters of exponentially damped/undamped sinusoids in noise. *Acoustics, Speech and Signal Processing, IEEE Transactions on*, 38(5):814–824, 1990.
- [20] Wenjing Liao and Albert Fannjiang. Music for single-snapshot spectral estimation: Stability and super-resolution. *Applied and Computational Harmonic Analysis*, 2014.
- [21] O. Michailovich and D. Adam. Robust estimation of ultrasound pulses using outlier-resistant de-noising. *Medical Imaging, IEEE Transactions on*, 22(3):368–381, March 2003.
- [22] O. Michailovich and A. Tannenbaum. Blind deconvolution of medical ultrasound images: A parametric inverse filtering approach. *Image Processing, IEEE Transactions on*, 16(12):3005–3019, Dec 2007.
- [23] O.V. Michailovich and D. Adam. A novel approach to the 2-d blind deconvolution problem in medical ultrasound. *Medical Imaging, IEEE Transactions on*, 24(1):86–104, Jan 2005.
- [24] Ankur Moitra. Super-resolution, extremal functions and the condition number of vandermonde matrices. *arXiv preprint arXiv:1408.1681*, 2014.
- [25] Richard Roy and Thomas Kailath. Esprit-estimation of signal parameters via rotational invariance techniques. *Acoustics, Speech and Signal Processing, IEEE Transactions on*, 37(7):984–995, 1989.
- [26] Ralph O Schmidt. Multiple emitter location and signal parameter estimation. *Antennas and Propagation, IEEE Transactions on*, 34(3):276–280, 1986.
- [27] Petre Stoica and Randolph L Moses. *Spectral analysis of signals*. Pearson/Prentice Hall Upper Saddle River, NJ, 2005.
- [28] Gongguo Tang, Badri Narayan Bhaskar, and Benjamin Recht. Sparse recovery over continuous dictionaries-just discretize. In *Signals, Systems and Computers, 2013 Asilomar Conference on*, pages 1043–1047, Nov 2013.
- [29] Gongguo Tang, Badri Narayan Bhaskar, Parikshit Shah, and Benjamin Recht. Compressed sensing off the grid. *Information Theory, IEEE Transactions on*, 59(11):7465–7490, 2013.
- [30] Ronen Tur, Yonina C Eldar, and Zvi Friedman. Innovation rate sampling of pulse streams with application to ultrasound imaging. *Signal Processing, IEEE Transactions on*, 59(4):1827–1842, 2011.
- [31] Noam Wagner, Yonina C Eldar, and Zvi Friedman. Compressed beamforming in ultrasound imaging. *Signal Processing, IEEE Transactions on*, 60(9):4643–4657, 2012.
- [32] Inger Wendelhag, Quan Liang, Tomas Gustavsson, and John Wikstrand. A new automated computerized analyzing system simplifies readings and reduces the variability in ultrasound measurement of intima-media thickness. *Stroke*, 28(11):2195–2200, 1997.
- [33] John Wikstrand. Methodological considerations of ultrasound measurement of carotid artery intima-media thickness and lumen diameter. *Clinical physiology and functional imaging*, 27(6):341–345, 2007.